RSC Advances

ROYAL SOCIETY OF CHEMISTRY

PAPER

View Article Online
View Journal | View Issue

Check for updates

Cite this: *RSC Adv.*, 2024, **14**, 21375

$Na_{0.4}MnO_2$/MXene nanocomposites as cathodes for high-performance aqueous zinc-ion batteries†

Guangquan Si,*[a] Wei Li, *[b] Taijiang Li,[b] Caixia Wang[b] and Qi Sun[b]

Received 16th April 2024
Accepted 2nd July 2024

DOI: 10.1039/d4ra02815e

rsc.li/rsc-advances

The distinctive configuration of MnO_2 renders it an exceptionally promising candidate for cathode materials for aqueous zinc-ion batteries (ZIBs). However, its practical utilization is constrained by the sluggish diffusion kinetics of Zn^{2+} and the capacity degradation resulting from lattice distortions occurring during charge and discharge cycles. To address these challenges, $Na_{0.4}MnO_2$@MXene with a typical 2 × 4 tunnel structure has been successfully synthesized by a simple hydrothermal method in the presence of 5 M NaCl. The nanorods are about 56 nm in diameter. The zinc-ion batteries (ZIBs) with $Na_{0.4}MnO_2$@MXene displays a specific capacity of 324.6 mA h g^{-1} at 0.2 A g^{-1}, and have a high reversible capacity of 153.8 mA h g^{-1} after 1000 charge–discharge cycles at 2 A g^{-1} with a capacity retention of 91.4%. The unique morphology endows abundant electrochemical active sites and facile ion diffusion kinetics, that contribute to the high specific capacity and stability. The $Na_{0.4}MnO_2$@MXene with a 2 × 4 tunnel structure is a promising candidate as an electrode material for ZIBs.

Introduction

Renewable energy sources such as tidal, solar and wind energy have gained the attention of people around the world with the deteriorating climate and pollution-prone environment.[1,2] However, these energy sources are intermittent and the pursuit of sustainable and efficient electrochemical energy storage technologies has been initiated.[3,4] The research of energy storage devices is the most effective way to achieve energy sustainability and reduce excessive greenhouse gas emissions. Therefore, lithium-ion batteries have been introduced into thousands of households, and the popularity of lithium batteries has brought some safety hazards and resource depletion.[5] Aqueous zinc-ion batteries (ZIBs) are based on nature's rich and abundant zinc resources, high-security aqueous electrolyte, and convenient battery assembly environment, which makes them the most likely alternative to lithium batteries as a new type of secondary battery.[6,7]

In spite of the above advantages, ZIBs are facing many challenges towards commercialisation, such as poor cycling stability of the cathode material, dissolution of the cathode material and zinc dendrites at the negative electrode.[8,9] To address these issues, we have been exploring suitable cathode materials, and manganese oxides are one of the most popular.[10,11] Composites of manganese oxides with carbon-based materials are a good option to enhance the electrical conductivity and charge transfer kinetics of manganese oxides, and so far a variety of carbon materials (graphene, carbon nanotubes, N-doped carbon, *etc.*) have been proved to be an ideal carrier electrochemistry for obtaining enhancement in manganese oxides.[12,13]

Currently, a new class of transition metal carbide/nitride $Ti_3C_2T_x$ (MXene) has become a new member of the two-dimensional material family.[14,15] Due to the presence of a layer of conducting carbon atoms and a layer of titanium metal in the structure of MXene, it is characterised by a large specific surface area, good metal conductivity and good hydrophilicity.[16] However, the energy storage performance of a single MXene material is low, and its layered structure is prone to spontaneous collapse and stacking. This limits the application and further development of this material in the field of energy storage.[17–19] In order to solve this problem, researchers have introduced battery-like materials with high specific capacity by introducing them between the MXene layers.[20,21] For example, Qiu *et al.*[22] designed a novel 3D high-density MnO_2/MXene composite electrode material, in which MnO_2 is wrapped between the folded MXene layers, effectively constructing a 3D conductive structure, which is conducive to the rapid transfer of ions and stable cycling. The capacity is 324.6 mA h g^{-1} at 0.2 A g^{-1}. Its excellent performance foretells its prospect in energy storage devices.

Based on this, in the present work, $Na_{0.4}MnO_2$@MXene nanorods with typical (2 × 4) tunneling structure were successfully synthesised by a simple hydrothermal method using two-dimensional material MXene nanosheets as a carrier. The diameter of the nanorods is about 56 nm. The specific capacity of ZIBs is 153.8 mA h g^{-1} with 91.4% capacity retention

---

[a] *Huaneng Power International, Inc., Beijing 100031, China. E-mail: liwei@tpri.com.cn*
[b] *Xi'an Thermal Power Research Institute Co., Ltd., Xi'an 710054, China*

† Electronic supplementary information (ESI) available. See DOI: https://doi.org/10.1039/d4ra02815e

after 1000 charge/discharge cycles at 1 A g^{-1}. The unique morphology endows the material with abundant electrochemical active sites and convenient ion diffusion kinetics, resulting in its high specific capacity and stability. $Na_{0.4}MnO_2$@MXene with (2 × 4) tunneling structure is promising as an electrode material for ZIBs. It was finally determined that the optimised $Na_{0.4}MnO_2$/MXene electrode material exhibited the best performance.

Experimental

Synthesis of few-layer MXene nanosheets

To synthesize few-layer MXene nanosheets, 1.6 g LiF was added to 20 mL solution (9 M HCl). Under magnetic stirring, 1 g of Ti_3AlC_2 powder was dissolved in the aforementioned etching solution and maintained at 30 °C for 48 h. (**Caution**: This step involves the generation of hydrogen fluoride and must be done inside the fume hood.) The black product was washed with deionized water until the pH of the supernatant reached around 6. The obtained clay-like sediment was redispersed in deionized water (200 mL) and ultrasonically processed at room temperature for 2 h under Ar flow to acquire ultrathin MXene nanosheets. The dispersion was centrifuged at 3000 rpm for 30 min to obtain the monolayer or few-layer MXene nanosheets by collecting the supernatant and freezedried

Synthesis of $Na_{0.4}MnO_2$@MXene

MXene nanosheets (30 mg) acquired were added to 50 mL H_2O, and was sonicated for 30 min at room temperature (A). Another solution 0.3 M $MnCl_2 \cdot 4H_2O$, 5 M NaOH and 0.1 M $KMnO_4$ in 50 mL H_2O was prepared (B). Then, A was dropped into B while being magnetically stirred, The solution was magnetically stirred at 60 °C for 12 h, and aged for 2 days. The precipitate was collected by centrifugation, and was washed with deionized water. The product was collected by freeze-drying to obtain layer structured Na-birnessite/MXene. Then, 0.1 g of Na-birnessite/MXene was homogeneously dispersed in NaCl (5 M 30 mL), it was placed it in to an autoclave and warmed for 16 hours at 180 °C. Centrifugation was used to separate the precipitates, repeatedly washed with deionized water, and the product is dried in an oven. The powder is named as $Na_{0.4}MnO_2$/MXene (NMO/MXene). The same procedure was used to prepare samples with the labels $Na_{0.4}MnO_2$ (NMO), NMO/MXene20, but different amounts of MXene powder were added: 0, 20 and 30 mg, respectively.

Material characterization

X-ray powder diffraction (XRD) patterns of the prepared materials were acquired by means of an X-ray powder diffractometer (Rigaku, D/Max-3c) under Cu Kα radiation ($\lambda = 0.15418$ nm); the morphology and elemental analysis (mapping) of the samples were characterized by field emission scanning electron microscopy (FE-SEM, Hitachi S-4800, Japan); the surface morphology and crystal structure of the prepared materials were further analyzed by transmission electron microscopy (Thermo Scientific, FEI Tecnai G2 F20) at an accelerating voltage of 200 kV; the composition and valence state of the prepared materials were measured by X-ray photoelectron spectrometer (Kratos, AXIS SUPRA+) and analyzed by Casa XPS software; the Raman spectra of the prepared materials were studied by the *in situ* confocal micro-Raman spectrometer (Horiba France, Lab RAM-HR); thermogravimetric analysis (TGA) was performed to identify the degradation pattern of the samples (after drying) from room temperature to 800 °C at a heating rate of 10 °C min^{-1} under air flow by the thermogravimetric analyzer (STA7200RV, Hitachi). The specific surface area and pore size of the samples were determined (Micromeritics, ASAP 2020) by the Brunuer–Emmett–Teller technique (BET).

Electrochemical characterization

CR2032 coin-type cells are utilized to test the electrochemical performance. The ink is prepared by mixing active material, super P and polypropylene fluoride (PVDF) binder in a weight ratio of 8 : 1 : 1 mixed with *N*-methyl-2-pyrrolidone (NMP) solvent. The mixture was then grounded to obtain a uniform slurry and drop coated on stainless steel foil. After drying overnight at 60 °C, a working cathode for Zn-ion batteries was obtained. The loading of the active material was controlled to 1.0 mg cm^{-2}. In addition, a piece of zinc foil and a glass fiber membrane (GF/A 1820) was used as the battery anode and the separator, respectively. Aqueous solutions of 2 M $ZnSO_4$ + 0.2 M $MnSO_4$ were used as electrolytes, and the addition of Mn^{2+} in the electrolyte can improve the cycling stability of the ZIB. 0.2 mL of electrolyte was added to each CR2032 battery. The cells were tested for electrochemical properties using Xinwei battery test system (CT-3008-5V10 mA) at different charge and discharge current densities from 200 to 3000 mA g^{-1} within the voltage limit of 1–1.9 V. Cyclic voltammetry (CV) testing and electrochemical impedance (EIS) analysis was performed by an electrochemical workstation (CHI660e). All electrochemical tests were performed at room temperature.

Results and discussion

The Na-birnessite/MXene was acquired by redox reaction of Mn^{2+} and MnO_4^- under an alkaline environment. The Na-birnessite@MXene with layered structure was transformed into a (2 × 4) tunnel structure using high concentration of NaCl etching. Using *in situ* produced HF to selectively etch the Al layers, followed by ultrasonication, the Ti_3AlC_2 MAX phase was exfoliated. During this process, the –OH and –F will be introduced to the surface of MXene nanosheets, which can attract Mn^{3+} and Mn^{4+} through electrostatic interactions. The hydrolysis and decomposition of NaOH creates an alkaline environment under solvothermal conditions, and the $Na_{0.4}MnO_2$ are formed and composite with the exfoliated MXene. Nuclei may be distributed on the MXene sheets at different locations and grow in different directions. Therefore, the formed $Na_{0.4}MnO_2$ nanorods are interwoven, resulting in a NMO@MXene composite with large specific surface area.

Fig. 1a–c shows the scanning electron microscope (SEM) images of the NMO@MXene at different magnifications. At low magnification, the microstructure of NMO@MXene is spherical aggregates with different sizes (0.5–5 μm), but at high magnification, the spherical aggregates are composed of nanorods, similar to the (2 × 4) tunneling structure of MnO_2 reported previously.[23] Fig. 1d is the transmission electron microscope (TEM) image of NMO@MXene, which shows nanorods with an average diameter of about 56 nm, consistent with the results shown in SEM images. Fig. 1e shows the electron diffraction spectroscopy (EDS) of Mn, Na, O and C elements. The uniform distribution of Mn, Na, O and C elements on the sample surface is consistent with the expected composition of NMO@MXene.

Fig. 2a showed the XRD patterns NMO, NMO@MXene and NMO@MXene20. For NMO, the diffraction peak at $2\theta = 6.1°$ and 13.6° can be assigned to the (002) and (200) crystal planes of the MnO_2 phase.[24,25] The strong peak intensity indicates high crystallinity. For NMO@MXene, after the MXene of doped, the diffraction peaks at $2\theta = 13.6°$, 24.7°, 32.3°, 37.6° and 66.2° of the NMO/MXene are shown, corresponding to (200), (400), (404), (600) and (002) planes, respectively.[26,27] NMO@MXene20 of the intensity of the peaks is low, which indicates the poor crystallinity of NMO@MXene20. Fig. 2b was the thermogravimetric curve (TGA) of NMO@MXene. The change in weight can be divided into three stages. In the first stage (30–180 °C), the weight of NMO@MXene decreases due to the evaporation of free water molecules adsorbed by NMO@MXene. The weight decline of NMO@MXene in the second stage (180–550 °C) is due to the gas formation of the bound water trapped in the tunnel structure of NMO@MXene, while the weight decline of NMO@MXene in the third stage (550–800 °C) is due to the release of lattice oxygen.The Raman spectra of NMO@MXene are shown in Fig. 2c. The Raman characteristic peaks of 638 cm^{-1} corresponded to the Mn–O characteristic peaks in the NMO@MXene tunnel structure.The Raman characteristic peak of 725 cm^{-1} and 2631 cm^{-1} corresponds to the MXene characteristic peak.[28] Fig. 2d displays the BET results of NMO@MXene. The N_2 adsorption–desorption isothermal curve of NMO@MXene belongs to type II, which is a material with large pores. The Brunauer–Emmertt–Teller (BET) test determined that NMO@MXene has a specific surface area of 84.6 $m^2\ g^{-1}$.

The surface chemical composition and physical properties of the NMO@MXene are determined by X-ray photoelectron spectroscopy (XPS). Fig. 3a shows that the Na 1s fitting peak is located at 1070.2 eV, which indicates the doping of Na and the ionic characteristics of Na in the structure of the samples. In the Mn 3s spectrum of Fig. 3b, the ΔE of the NMO@MXene is 5.1 eV. The indicate that the transformation of Na-birnessite@MXene layer structure into NMO@MXene tunnel structure would cause the change of electron binding energy, which results in a difference between the average oxidation states. As shown in Fig. 3c, the Mn 2p spectrum can be fitted to four peaks. The Mn 2p peaks at 643.8 and 654.2 eV are associated to the Mn $2p_{3/2}$ and Mn $2p_{1/2}$ of Mn^{4+}, respectively. The Mn 2p peaks near 641.6 and 653.1 eV are associated to the Mn $2p_{3/2}$ and Mn $2p_{1/2}$ peaks of Mn^{3+}, respectively.[29] Therefore, in the NMO@MXene, Mn appears in the form of Mn^{3+} and Mn^{4+}, and the spin–orbit splitting energy (ΔE) of Mn $2p_{3/2}$ and Mn $2p_{1/2}$ is 11.7 eV, which

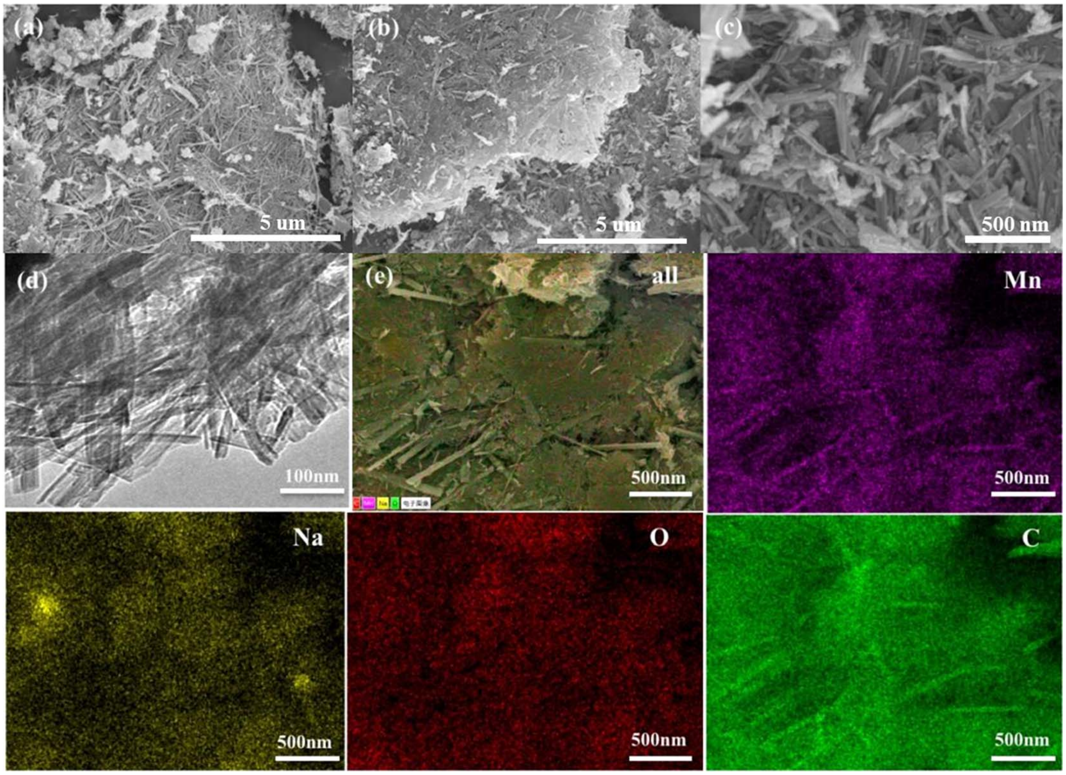

Fig. 1 SEM images of the (a, b and c) NMO@MXene; (d) TEM images of the NMO@MXene; (e) EDS elemental mapping of the NMO@MXene.

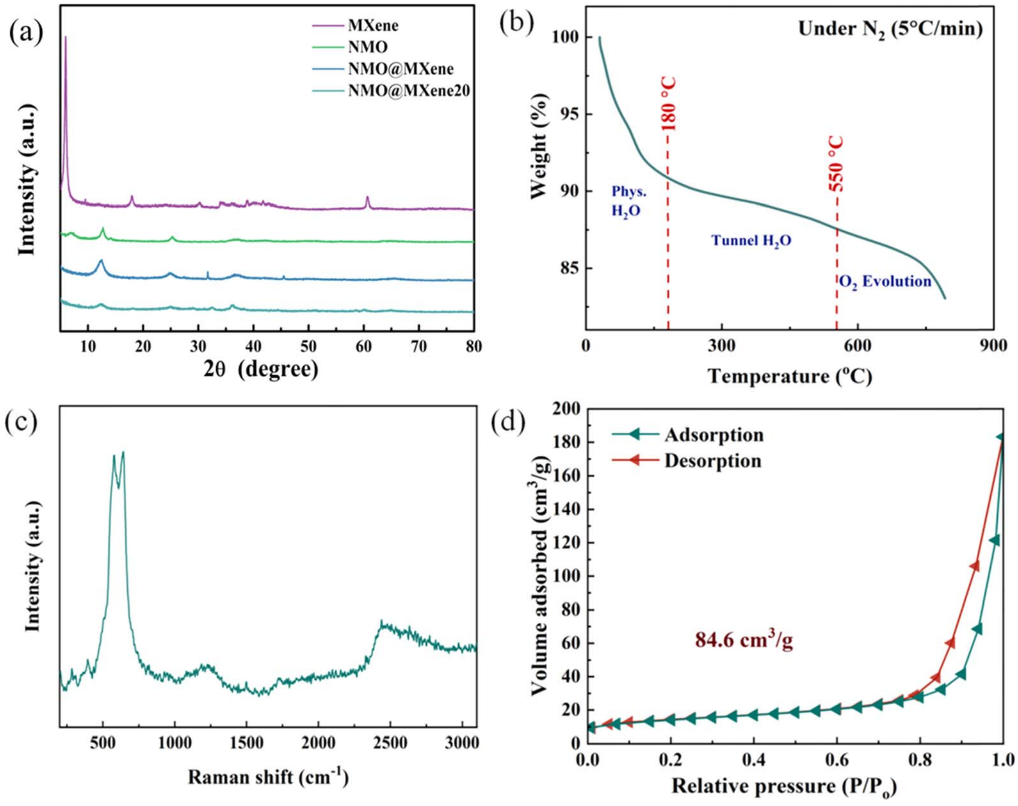

Fig. 2 (a) XRD patterns of NMO, NMO@MXene and NMO/MXene20; (b) thermogravimetric analysis (TGA) profile under N_2; (c) Raman spectra of NMO@MXene; (d) BET pattern of NMO@MXene.

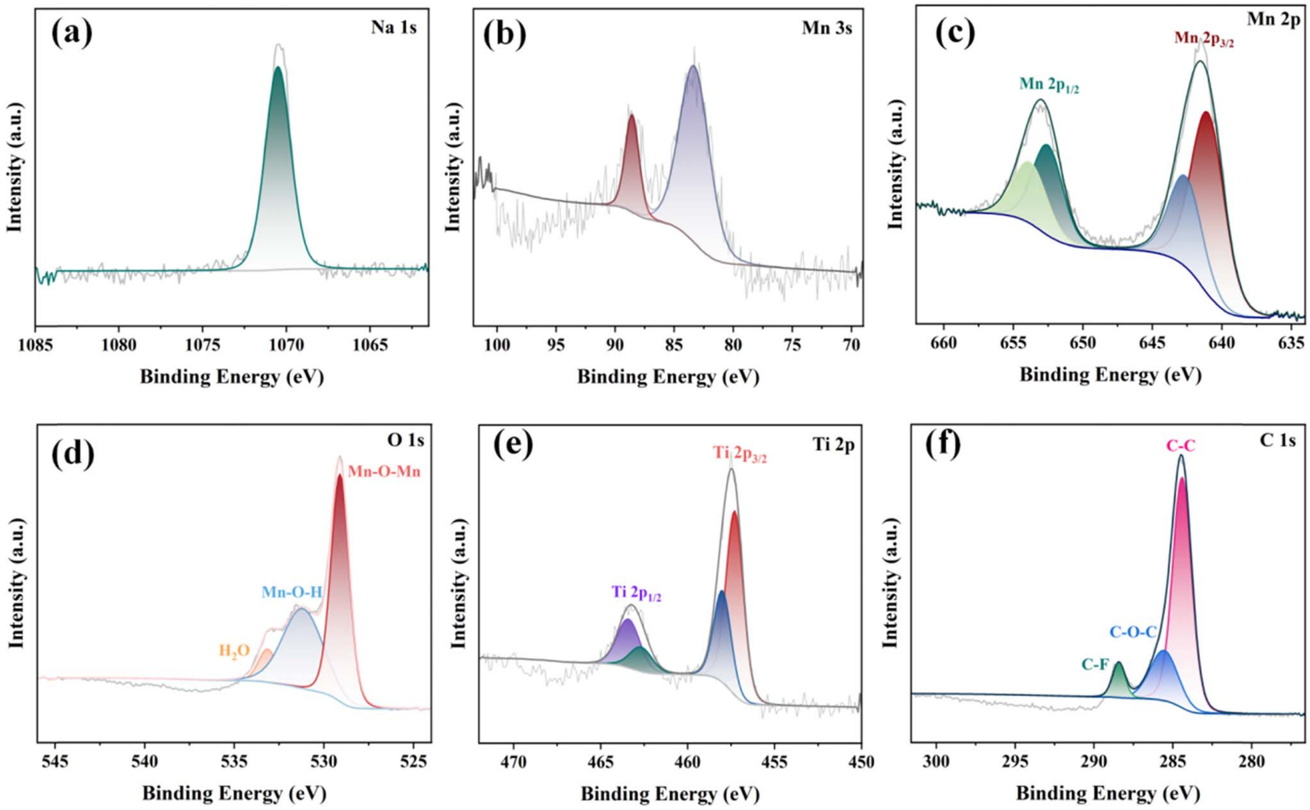

Fig. 3 Deconvoluted high-resolution XPS spectra of the (a) Na 1s region; (b) Mn 3s region; (c) Mn 2p region; (d) O 1s region; (e) Ti 2p region; and (f) C 1s region of the NMO@MXene.

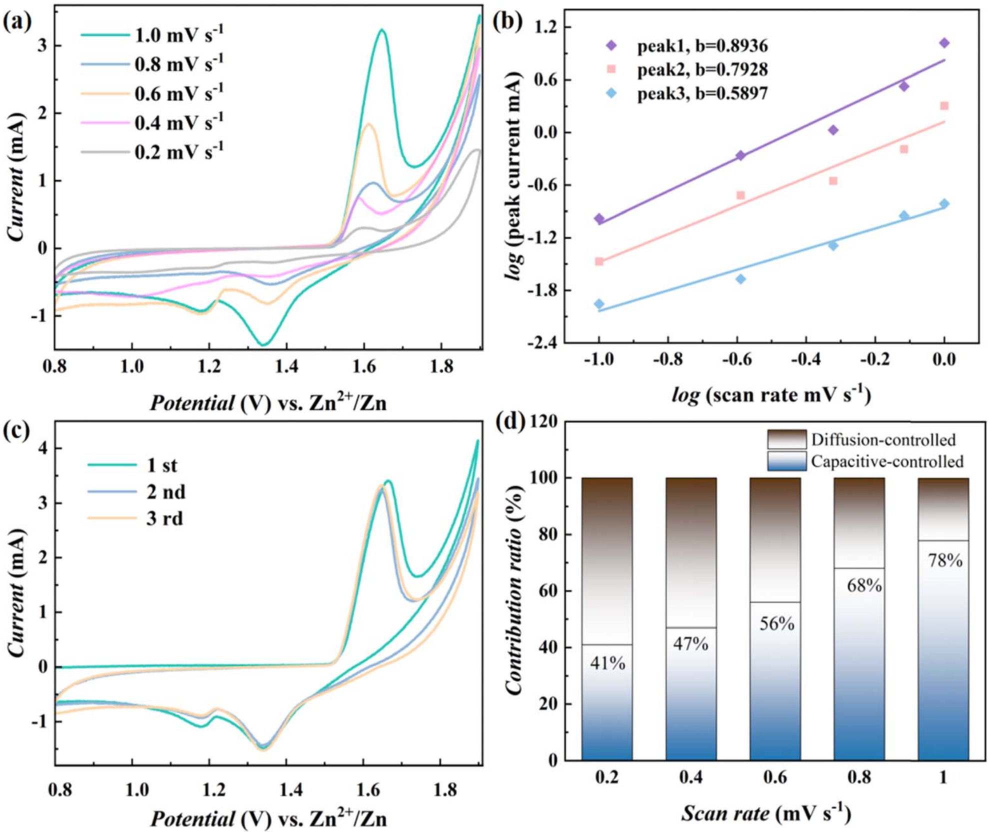

Fig. 4 (a) CV curves of the ZIBs with NMO@MXene at various scan rates; (b) determination of the *b* value according to log *i* and log *v* plots; (c) CV curves of the ZIBs with NMO@MXene at 0.2 mV S^{-1}; (d) contribution ratios of capacitive-like and diffusion-controlled processes at different scan rates.

is consistent with MnO_2 reported in the related literature.[30] Fig. 3d shows the deconvolution high-resolution XPS spectra of the O 1s region. In addition to the Mn–O–Mn and Mn–O–H located at the main peaks of 529.7 and 531.7 eV, respectively, H–O–H fitting peaks due to surface adsorbed water also appears at 533.2 eV. Combined with the SEM, TEM, XRD, XPS and Raman spectroscopy, the NMO@MXene successfully preparated manganese oxide nanocomposites with (2 × 4) tunnel structure using sodium ion as the guiding agent. Fig. 3e shows the high-resolution XPS spectrum of Ti 2p. It have two obvious main peaks representing the Ti $2p_{3/2}$ and Ti $2p_{1/2}$ orbits. These main peaks can be convolutioned into four peaks, Ti^{2+} ($2p_{3/2}$ 456.48 eV and $2p_{1/2}$ 462.88 eV) and Ti^{3+} ($2p_{3/2}$ 458.73 eV and $2p_{1/2}$ 463.08 eV). Fig. 3f three main peaks can be fitted to the C 1s spectrum shown in Fig. 3c, with and C–F, C–O–C and C–C bonds attributable to peaks at 288.7, 286.1 and 284.6 eV, respectively.

Coin-type (CR2032) aqueous ZIBs are assembled using NMO@MXene or the NMO as the cathode and zinc foil as the anode, 2 M $ZnSO_4$ + 0.2 M $MnSO_4$ solution as electrolyte. Fig. 4a shows the measured CV of ZIB with NMO@MXene at different scan rates. There is a linear relationship between the peak current (*i*) and the scan rate (*v*), which can reflect the charge storage process.[31]

$$\log i - b \log v + \log a \tag{1}$$

$$i(v) = k_1 v | k_2 v^{1/2} \tag{2}$$

In eqn (1) and (2), *a* and *b* are the parameters in formula (1), and the *b* value represents the slope of log *i* *vs.* log *v*. When the *b* value is close to 0.5, it indicates that the diffusion-controlled process is dominant. When the *b* value is close to 1, it is related to the surface capacitance-controlled process. The *b* values of peak 1, peak 2 and peak 3 fitted in Fig. 4b are 0.8936, 0.7928, and 0.5897, respectively, which indicates that the electrochemical reaction process that occurs in ZIBs with NMO@MXene is mainly based on capacitance-controlled processes. The stored charge can then be decomposed into diffusion and surface capacitive contributions according to eqn (2), and k_1 and k_2 are constants relating to these contributions.

The Zn^{2+} storage behavior of the ZIBs is evaluated by CV. Fig. 4c shows the CV of the first three cycles of the ZIBs with NMO@MXene at 0.1 mV s^{-1}. During the first cycle, the initial cathodic scan shows a broad reduction peaks at 1.19 and 1.32 V, which is due to the insertion of Zn^{2+} and H^+, with the reduction of Mn^{4+}. At the anodic scan, sharp oxidation peaks at 1.63 is associated with the extraction of Zn^{2+} and H^+ and the formation of Mn^{4+}. During the subsequent cycle, the peak current and peak potential of the reduction peak remain unchanged, while the

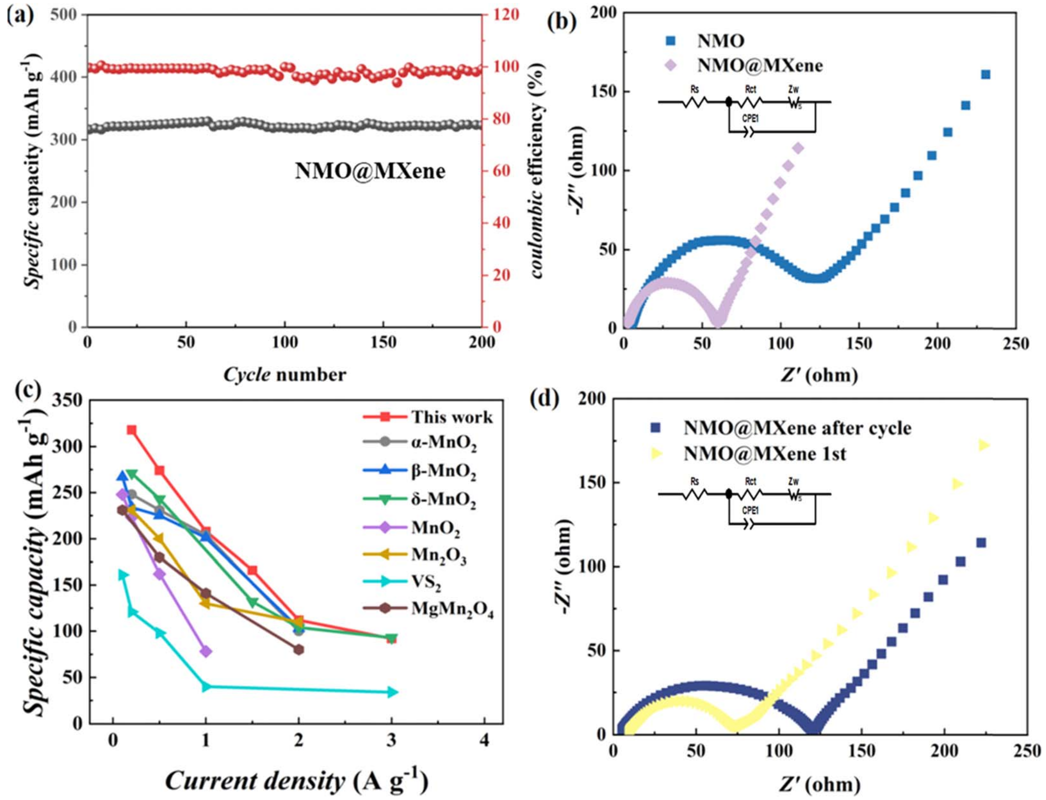

Fig. 5 (a) Cycle performance at 0.2 A g^{-1}; (c) the specific capacity of the ZIBs with NMO@MXene and other reported cathodes; (b) and (d) Nyquist plots and of the ZIBs with NMO@MXene.

peak current of the oxidation peak gradually decreases and the peak potential shifts negatively. The initial CV of ZIBs basically overlap, which indicates that the ZIB with NMO@MXene has low polarization and high reversibility. From Fig. 4d, the capacitive contribution of ZIB with $Na_{0.4}MnO_2$ increases from 41% to 78% when the scan rate increases from 0.2 to 1 mV s^{-1}.

The specific capacity of ZIB with NMO@MXene does not change when the current density is 0.2 A g^{-1} after 200 cycles, the ZIB with NMO@MXene shows a higher reversible capacity, as shown in Fig. 5a. Fig. 5d shows ZIBs with NMO@MXene is compared with previously reported ZIBs with α-MnO_2,[13] β-MnO_2,[12] δ-MnO_2,[15] MnO_2,[32] Mn_2O_3,[33] VS_2 (ref. 34) or $MgMn_2O_4$.[35] The ZIB with NMO@MXene shows higher specific capacity. The electrochemical impedance spectra of ZIBs with NMO@MXene or NMO electrodes are measured as shown in Fig. 5b and d. According to the fitting results, ZIBs with NMO@MXene showed lower R_{ct}, which indicates that structure of NMO@MXene has a more facile charge storage kinetics. The conductive MXene nanosheets facilitate rapid electron transport, while $Na_{0.4}MnO_2$ possesses an enlarged crystal tunnel size, contributing to enhanced ion diffusion kinetics. Consequently, the synergistic interaction between these two components endows NMO@MXene with superior electrochemical performance in Zn-ion batteries.

Fig. 6a shows the rate performance of ZIBs tested under different current densities. The ZIB with NMO@MXene has an initial capacity of 324.6 mA h g^{-1} when the current density is 0.2 A g^{-1}, and the specific capacity decreases continuously as the current density increases. When the current densities are 0.5, 1, 2 and 3 A g^{-1}, the capacities are 275.2, 214.7, 166.3 and 95.3 mA h g^{-1}, respectively. The capacities of ZIBs with NMO electrodes at 0.2, 0.5, 1, 2 and 3 A g^{-1} are 276.4, 256.5, 235.7, 188.5 and 82.4 mA h g^{-1}, respectively. When the current density returns to 0.2 A g^{-1}, the capacities of the two ZIBs return to their initial values. The specific capacity of ZIB with NMO@MXene decreases slightly when the current density is 3 A g^{-1} after 160 cycles. The ZIB with NMO@MXene shows a higher reversible capacity. As shown in Fig. 6b. When the current density rises to 2 A g^{-1} (Fig. 6c), the ZIB with NMO@MXene exhibits a specific capacity of 153.8 mA h g^{-1} after 1000 cycles. The capacity retention rate is 91.4%, and the Coulomb efficiency is close to 100%. The capacity of ZIB with NMO electrode is only 101.3 mA h g^{-1} after long cycle at 2 A g^{-1}, and the capacity retention rate is 66.2%. Therefore, the ZIB with NMO@MXene exhibits higher reversible capacity and better stability than ZIB with NMO electrodes. Additionally, MXene's high specific surface area serves as an effective substrate for the deposition of Mn^{2+} from the electrolyte, mitigating the capacity loss due to Mn dissolution during discharge. This attribute significantly contributes to the excellent cycle stability observed in NMO@MXene.

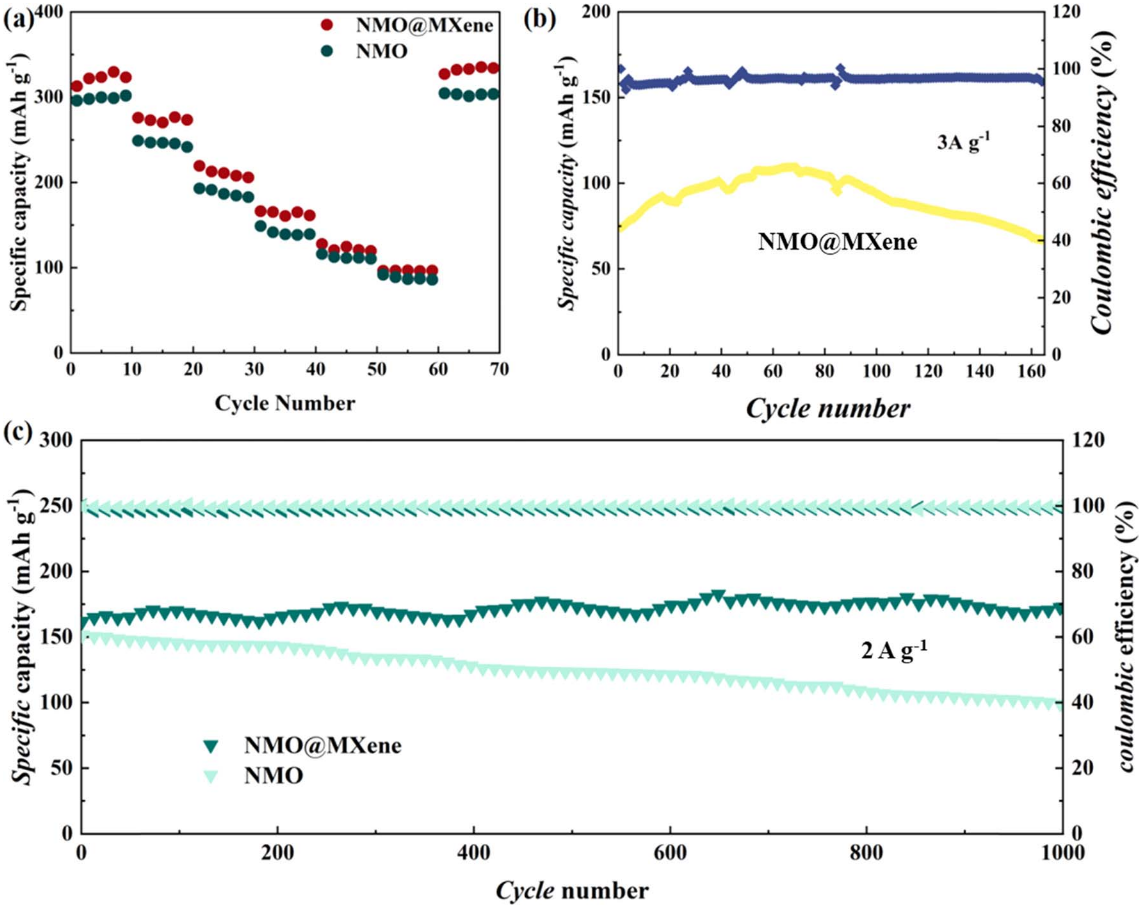

Fig. 6 (a) Rate performances of ZIBs with NMO@MXene and NMO; cycling performance at 3 A g^{-1} (b), and long-term cycling performance at 2.0 A g^{-1} (c) of the ZIBs with NMO@MXene and NMO.

Conclusion

The (2 × 4) tunneling structure $Na_{0.4}MnO_2$@MXene nanocomposites are synthesized by converting the layered Na-birnessite@MXene by a hydrothermal method in the presence of NaCl. When used as the cathode material for ZIBs, a high specific capacity of 324.6 mA h g^{-1} at a current density of 0.2 A g^{-1} is achieved. The ZIB with NMO@MXene shows superior cycling stability, with a capacity retention of 91.4% and a coulombic efficiency nearly 100% after 1000 GCD cycles at 2 A g^{-1}. Both diffusion-controlled processes and surface-capacitive controlled processes contribute to the charge-storage mechanism. The superior charge storage performance is originated from the increased number of electrochemically active sites and more facile ion diffusion kinetics. Both the crystalline structure and the nanorod morphology remain stable during charging and discharging, and evidence of both H^+ and Zn^{2+} insertion is observed. These results indicate that $Na_{0.4}MnO_2$@MXene nanocomposites with (2 × 4) tunneling structure can be used as a promising cathode material for ZIBs. In addition, transformation of crystal structures of manganese-based materials induced by high concentration of metal cation and MXene doping is an effective route to improve their electrochemical performance.

Data availability

The datasets generated during and/or analysed during the current study are available from the corresponding author on reasonable request. The data supporting this article have been included as part of the ESI.†

Author contributions

G. Q. S.: investigation, data curation, visualization, writing-original draft. W. L.: conceptualization, funding acquisition, supervision. T. J. L.: investigation, data curation, visualization. C. X. W.: software, methodology. Q. S.: conceptualization, supervision, guidance, writing-reviewing and editing.

Conflicts of interest

The authors declare that they have no known competing financial interests or personal relationships that could have appeared to influence the work reported in this paper.

Acknowledgements

Authors thank the funding from Science and Technology Project of China Huaneng Group Co., Ltd. (HNKJ23-HF55);

Science and Technology Project of China Huaneng Group Co., Ltd. (HNKJ22-H78).

References

1 V. L. Chevrier, L. Liu, R. Wohl, A. Chandrasoma, J. A. Vega, K. W. Eberman, P. Stegmaier and E. Figgemeier, *J. Electrochem. Soc.*, 2018, **165**, A1129.

2 Y.-P. Deng, R. Liang, G. Jiang, Y. Jiang, A. Yu and Z. Chen, *ACS Energy Lett.*, 2020, **5**, 1665–1675.

3 Y. An, Y. Tian, Y. Zhang, C. Wei, L. Tan, C. Zhang, N. Cui, S. Xiong, J. Feng and Y. Qian, *ACS Nano*, 2020, **14**, 17574–17588.

4 R. Schmuch, R. Wagner, G. Hörpel, T. Placke and M. Winter, *Nat. Energy*, 2018, **3**, 267–278.

5 B. Tang, L. Shan, S. Liang and J. Zhou, *Energy Environ. Sci.*, 2019, **12**, 3288–3304.

6 J. Qian, C. Wu, Y. Cao, Z. Ma, Y. Huang, X. Ai and H. Yang, *Adv. Energy Mater.*, 2018, **8**, 1702619.

7 N. Zhang, X. Chen, M. Yu, Z. Niu, F. Cheng and J. Chen, *Chem. Soc. Rev.*, 2020, **49**, 4203–4219.

8 O. Ghodbane, J.-L. Pascal and F. Favier, *ACS Appl. Mater. Interfaces*, 2009, **1**, 1130–1139.

9 X. Wang, G. Tan, Y. Bai, F. Wu and C. Wu, *Electrochem. Energy Rev.*, 2021, **4**, 35–66.

10 M. Han, L. Qin, Z. Liu, L. Zhang, X. Li, B. Lu, J. Huang, S. Liang and J. Zhou, *Mater. Today Energy*, 2021, **20**, 100626.

11 A. S. Poyraz, W. Song, D. Kriz, C.-H. Kuo, M. S. Seraji and S. L. Suib, *ACS Appl. Mater. Interfaces*, 2014, **6**, 10986–10991.

12 M. Liu, Q. Zhao, H. Liu, J. Yang, X. Chen, L. Yang, Y. Cui, W. Huang, W. Zhao and A. Song, *Nano Energy*, 2019, **64**, 103942.

13 B. Wu, G. Zhang, M. Yan, T. Xiong, P. He, L. He, X. Xu and L. Mai, *Small*, 2018, **14**, 1703850.

14 D. Wang, L. Wang, G. Liang, H. Li, Z. Liu, Z. Tang, J. Liang and C. Zhi, *ACS Nano*, 2019, **13**, 10643–10652.

15 M. H. Alfaruqi, V. Mathew, J. Gim, S. Kim, J. Song, J. P. Baboo, S. H. Choi and J. Kim, *Chem. Mater.*, 2015, **27**, 3609–3620.

16 C. Yuan, Y. Zhang, Y. Pan, X. Liu, G. Wang and D. Cao, *Electrochim. Acta*, 2014, **116**, 404–412.

17 L. Wu, F. Xu, Y. Zhu, A. B. Brady, J. Huang, J. L. Durham, E. Dooryhee, A. C. Marschilok, E. S. Takeuchi and K. J. Takeuchi, *ACS Nano*, 2015, **9**, 8430–8439.

18 A. S. Poyraz, J. Huang, S. Cheng, D. C. Bock, L. Wu, Y. Zhu, A. C. Marschilok, K. J. Takeuchi and E. S. Takeuchi, *Green Chem.*, 2016, **18**, 3414–3421.

19 C.-H. Kim, Z. Akase, L. Zhang, A. H. Heuer, A. E. Newman and P. J. Hughes, *J. Solid State Chem.*, 2006, **179**, 753–774.

20 S. P. Nagalingam and A. N. Grace, *Mater. Today Chem.*, 2022, **26**, 101113.

21 M. Das, H. Murari, S. Ghosh and B. Sanyal, *Nanoscale*, 2024, **16**, 1352–1361.

22 W. Qiu, Y. Li, A. You, Z. Zhang, G. Li, X. Lu and Y. Tong, *J. Mater. Chem. A*, 2017, **5**, 14838–14846.

23 Z.-h. Liu and K. Ooi, *Chem. Mater.*, 2003, **15**, 3696–3703.

24 L. Kang, Z.-H. Liu, Z. Yang and K. Ooi, *Mater. Lett.*, 2006, **60**, 3565–3568.

25 H. Huang, C.-H. Chen, L. Xu, H. Genuino, J. Garcia-Martinez, H. F. Garces, L. Jin, C. K. o. Kithongo and S. L. Suib, *Chem. Commun.*, 2010, **46**, 5945–5947.

26 K. Kuratani, K. Tatsumi and N. Kuriyama, *ECS Trans.*, 2008, **6**, 279.

27 X. Zhang, X. Sun, H. Zhang, C. Li and Y. Ma, *Electrochim. Acta*, 2014, **132**, 315–322.

28 M. Zhao, Y. Luo, L. Zhu, D. Cai, Y. Zhuang, Q. Chen and H. Zhan, *J. Alloys Compd.*, 2022, **913**, 165124.

29 J. Wang, J. G. Wang, H. Liu, Z. You, Z. Li, F. Kang and B. Wei, *Adv. Funct. Mater.*, 2021, **31**, 2007397.

30 M. Lin, F. Shao, Y. Tang, H. Lin, Y. Xu, Y. Jiao and J. Chen, *J. Colloid Interface Sci.*, 2022, **611**, 662–669.

31 C. Yang, J. Chen, X. Ji, T. P. Pollard, X. Lü, C.-J. Sun, S. Hou, Q. Liu, C. Liu and T. Qing, *Nature*, 2019, **569**, 245–250.

32 J. P. Tafur, J. Abad, E. Román and A. J. F. Romero, *Electrochem. Commun.*, 2015, **60**, 190–194.

33 N. Liu, X. Wu, Y. Yin, A. Chen, C. Zhao, Z. Guo, L. Fan and N. Zhang, *ACS Appl. Mater. Interfaces*, 2020, **12**, 28199–28205.

34 Y. Mao, J. Bai, J. Si, H. Ma, W. Li, P. Wang, H. Zhang, Z. Sheng, X. Zhu and P. Tong, *Mater. Horiz.*, 2023, **10**, 3162–3173.

35 V. Soundharrajan, B. Sambandam, S. Kim, V. Mathew, J. Jo, S. Kim, J. Lee, S. Islam, K. Kim and Y.-K. Sun, *ACS Energy Lett.*, 2018, **3**, 1998–2004.